Cavity-enhanced Raman emission from a single color center in a solid

Shuo Sun[1‡*], Jingyuan Linda Zhang[1‡], Kevin A. Fischer[1‡], Michael J. Burek[2],
Constantin Dory[1], Konstantinos G. Lagoudakis[1], Yan-Kai Tzeng[3], Marina Radulaski[1],
Yousif Kelaita[1], Amir Safavi-Naeini[1], Zhi-Xun Shen[3,4,5], Nicholas A. Melosh[4,5],
Steven Chu[3,6], Marko Lončar[2], and Jelena Vučković[1]

[1]E. L. Ginzton Laboratory, Stanford University, Stanford, California 94305, USA
[2]School of Engineering and Applied Sciences, Harvard University, Cambridge, Massachusetts 02138, USA
[3]Department of Physics, Stanford University, Stanford, California 94305, USA
[4]Geballe Laboratory for Advanced Materials, Stanford University, Stanford, California 94305, United States
[5]Stanford Institute for Materials and Energy Sciences, SLAC National Accelerator Laboratory, Menlo Park, California 94025, USA
[6]Department of Molecular and Cellular Physiology, Stanford University, Stanford, California 94305, USA
‡These authors contributed equally
*Email: shuo@stanford.edu

Abstract

We demonstrate cavity-enhanced Raman emission from a single atomic defect in a solid. Our platform is a single silicon-vacancy center in diamond coupled with a monolithic diamond photonic crystal cavity. The cavity enables an unprecedented frequency tuning range of the Raman emission (100 GHz) that significantly exceeds the spectral inhomogeneity of silicon-vacancy centers in diamond nanostructures. We also show that the cavity selectively suppresses the phonon-induced spontaneous emission that degrades the efficiency of Raman photon generation. Our results pave the way towards photon-mediated many-body interactions between solid-state quantum emitters in a nanophotonic platform.

Integration of solid-state quantum emitters with nanophotonic structures offers a scalable quantum photonics platform [1] that is essential for photonic quantum simulation [2], quantum metrology [3], quantum repeaters [4], and quantum networks [5,6]. However, despite significant progress in coupling single solid-state qubits with photons [7-10] and entangling two qubits [11-15], a scalable quantum photonic circuit consisting of many quantum emitters remains an outstanding challenge. One major obstacle towards this goal is the spectral inhomogeneity of solid-state quantum emitters [16], which limits their prospects in realizing many-body interactions through exchange of photons [5]. The ability to tune the emission frequency of a solid-state quantum emitter across the full range of inhomogeneous broadening remains a key missing ingredient in developing scalable quantum photonic circuits.

Color centers in solids have recently shown great promise for applications in scalable quantum photonic circuits, largely owing to their narrow spectral inhomogeneity. One of the candidates that has attracted significant interests in recent years is the negatively charged silicon-vacancy (SiV^-) center in diamond. SiV^- centers possess narrow inhomogeneous broadening on the order of 1 GHz in high quality diamond [17,18]. They also exhibit many other properties that are promising as optically accessible quantum memories, including high spectral stability [17], large zero-phonon-line emission (>70%) [19], gigahertz coupling strength with nano-cavities [14,20], as well as milliseconds spin coherence time [21]. Recent experiments have demonstrated photon-mediated entanglement between two SiV^- centers in a bare waveguide [14], where Raman emissions with a tuning range of 10 GHz were employed to compensate the spectral inhomogeneity of SiV^- centers. However, there are two main limitations in using this approach towards realizing photon-mediated

2

many-body interactions. First, once embedded in nanostructures, SiV$^-$ centers display a much larger spectral inhomogeneity (>20 GHz) than bulk due to local variations of the strain [22]. Second, the observed Raman emission is accompanied with a strong spontaneous emission from the same branch of the Λ-system [14], which fundamentally limits the efficiency of Raman photon generation and the fidelity of many-body interactions. To address both challenges requires selective enhancement of the Raman emission while suppressing the undesired spontaneous emission.

In this Letter, we demonstrate cavity-enhanced Raman emission from a single color center. Optical cavities have been utilized before to enhance Raman emission from a single semiconductor quantum dot, which enables the generation of single-photons with large tuning bandwidth [23] and variable pulse shape [24,25]. However, the cavity-enhanced tuning range remains two orders of magnitude smaller compared with the spectral inhomogeneity of quantum dots [26]. Here, we show that an optical cavity enables a frequency tuning range of 100 GHz for Raman emission from a single SiV$^-$ center, which is an order of magnitude larger than previously achieved with color centers and far exceeds the typical spectral inhomogeneity of SiV$^-$ centers in nanostructures. In addition, we provide a quantitative model to explain the undesired spontaneous emission by accounting for electron-phonon interactions, and show that the cavity can selectively suppress the spontaneous emission process and only enhance the Raman photon generation. Our results will facilitate the implementation of scalable quantum circuits and quantum networks that involve multiple solid-state quantum emitters in an integrated nanophotonic platform.

Figure 1(a) shows the energy level structure of a single SiV$^-$ center [27]. In the absence of a

3

magnetic field, the SiV$^-$ center contains two ground states separated by δ_g, and two excited states separated by δ_e. The values of δ_g and δ_e are $\delta_g/2\pi = 50\,\text{GHz}$ and $\delta_e/2\pi = 260\,\text{GHz}$ respectively [27], but they increase significantly in the presence of strain [28,29]. We utilize the Λ-system formed by the lower excited state (labeled as $|e\rangle$) and the two ground states (labeled as $|g_1\rangle$ and $|g_2\rangle$) to generate tunable Raman emission. We optically drive transition $|g_1\rangle \leftrightarrow |e\rangle$ with a continuous-wave laser, and couple transition $|g_2\rangle \leftrightarrow |e\rangle$ with a cavity. The driving Rabi frequency and the emitter-cavity coupling strength are denoted as Ω and g respectively. We set the detuning between the driving laser and transition $|g_1\rangle \leftrightarrow |e\rangle$ to be identical to the detuning between the cavity and transition $|g_2\rangle \leftrightarrow |e\rangle$ (both are given by Δ) in order to achieve Raman resonance [30-32].
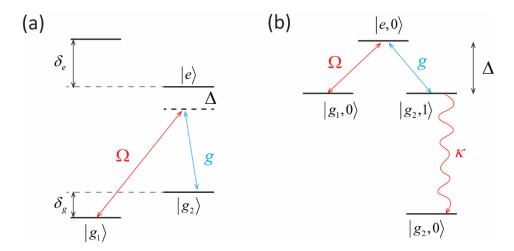

FIG. 1. (Color online) (a) Energy level structure of a SiV$^-$ center. The red arrow indicates the classical driving field, the blue arrow indicates the coupling with a cavity. (b) Energy level structure of the emitter-cavity system in the interaction picture and weak excitation regime.

To understand how we generate cavity-enhanced Raman emission, we illustrate the level

structure in the interaction picture as shown in Fig. 1(b). We denote each state in the form $|x,n\rangle$, where $x \in \{g_1, g_2, e\}$ is the state of the SiV$^-$ center, and $n \in \{0,1\}$ is the number of photons in the cavity. Here we consider the system in the weak excitation regime where the whole system contains at most one excitation – this truncation of the level structure is valid as long as $\Omega, g \ll \Delta$. Under the same assumption, we can also adiabatically eliminate the state $|e,0\rangle$, and treat the system as two-levels $|g_1,0\rangle$ and $|g_2,1\rangle$ driven by an effective Rabi frequency $\Omega_{eff} = \Omega g/\Delta$. Thus, if the system is initially in the state $|g_1,0\rangle$, it will coherently rotate to the state $|g_2,1\rangle$ followed by a photon emission through the cavity. The emission frequency is tunable with Δ because it does not involve any real excitation of the state $|e,0\rangle$.

The coupling between the emitter and the cavity enhances the rate of the Raman emission. Here we define the Raman emission rate as the inverse of the average time it takes to emit a photon when the system is initially in the state $|g_1,0\rangle$. In Supplementary Materials [33], we demonstrate that the cavity-enhanced Raman emission rate is given by $R_c = \dfrac{\Omega_{eff}^2}{\kappa} = \dfrac{g^2}{\kappa} \cdot \left(\dfrac{\Omega}{\Delta}\right)^2$, while the upper bound of the Raman emission rate without a cavity is given by $R_0 = \dfrac{(\Omega/2)^2}{\Delta^2 + (\Gamma/2)^2} \cdot \Gamma$, where Γ is the spontaneous emission rate of transition $|e\rangle \to |g_2\rangle$. In the limit where $\Delta \gg \Gamma$, the Raman emission rate is enhanced by a factor $\dfrac{R_c}{R_0} = \dfrac{4g^2}{\kappa\Gamma}$, which is the Purcell factor of the coupled emitter-cavity system. For SiV$^-$ centers, the Purcell factor can be more than a factor of 10 [20], corresponding to at least an order of magnitude enhancement of the Raman emission rate.

We couple a single SiV$^-$ center with a monolithic diamond nanobeam photonic crystal cavity.

Figure 2(a) shows a scanning electron microscope image of the fabricated photonic crystal cavity. The device fabrication starts with homoepitaxial growth of a thin layer of diamond on a single crystal diamond substrate using microwave plasma chemical vapor deposition [34]. We then fabricate nanobeam photonic crystal cavities using electron beam lithography followed by angled etching of the bulk diamond to create a suspended nanobeam [35,36]. Ref. [20] provides detailed information about the device design and fabrication.

We mount our sample in a closed-cycle cryostat (Montana Instruments) and cool it down to 4 K. We first measure the bare cavity transmission spectrum using a supercontinuum source. During the measurement we keep the cavity red-detuned from all transitions of the SiV$^-$ center by more than 40 cavity linewidths via controlled condensation of Argon gas [20]. The blue dots in Fig. 2(b) show the measured cavity spectrum. By fitting the measured data to a Lorentzian function (red solid line), we obtain a cavity energy decay rate of $\kappa/2\pi = 53.7 \pm 0.4 \, \text{GHz}$ (corresponding to a cavity quality factor of 7600).

Figure 2(c) shows the photoluminescence spectrum of the SiV$^-$ center embedded in the cavity. During the measurement we again keep the cavity red-detuned by more than 40 linewidths from the SiV$^-$ center. We observe four distinct peaks in the photoluminescence spectrum, labeled as A – D in the figure, corresponding to the four possible optical transitions of a single SiV$^-$ center. The peaks C and D correspond to transitions $|g_1\rangle \leftrightarrow |e\rangle$ and $|g_2\rangle \leftrightarrow |e\rangle$ respectively. From the frequency splitting between the emission peaks C and D, we calculate that $\delta_g/2\pi = 544 \, \text{GHz}$. This value is significantly larger compared with typical values of 50 GHz in the bulk, suggesting large residual strain in the nanobeam photonic crystals after nanofabrication. Second order correlation

measurements verify that the emissions from both peaks C and D exhibit clear anti-bunching and are therefore originated from a single SiV⁻ center [33]. We attribute the weak emission peak near transition C to a different emitter.
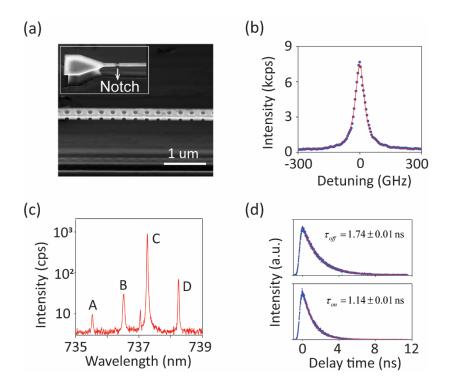

FIG. 2. (Color online) (a) Scanning electron microscope image of a fabricated nanobeam photonic crystal cavity in diamond. The inset shows the intentionally placed notch at the end of the nanobeam that couples light into the freestanding waveguide. (b) Transmission spectrum of a bare cavity measured using a supercontinuum source. (c) Photoluminescence spectrum of the SiV⁻ center we used in our experiment. (d) Lifetime measurement of the lower excited state of the SiV⁻ center when the cavity is far detuned from the emitter (upper panel) and when the cavity is resonantly coupled with transition $|g_2\rangle \leftrightarrow |e\rangle$ (lower panel). In both panel (b) and (d), blue dots show the measured data, the red solid lines show the numerical fit.

To characterize the coupling strength g between the cavity and transition $|g_2\rangle \leftrightarrow |e\rangle$, we measure the lifetime of the excited state $|e\rangle$ both when the cavity is far detuned and resonant with

the transition $|g_2\rangle \leftrightarrow |e\rangle$. The blue dots in Fig. 2(d) show the measured emission intensity as a function of the delay time between the emission and the excitation pulse. The upper and lower panels show the cases when the cavity is far detuned and on resonance with transition $|g_2\rangle \leftrightarrow |e\rangle$ respectively. By fitting the measured data to an exponential function (red solid line), we determine the lifetime of the excited state $|e\rangle$ to be $\tau_{off} = 1.74 \pm 0.01$ ns for the far detuned case, and $\tau_{on} = 1.14 \pm 0.01$ ns for the resonant case. We thus calculate the coupling strength to be $g/2\pi = 0.80 \pm 0.01$ GHz using the relation $\frac{1}{\tau_{on}} = 4g^2/\kappa + \frac{1}{\tau_{off}}$. We also estimate a lower-bound Purcell factor of 20 [33].

We now demonstrate cavity-enhanced Raman emission. We excite the transition $|g_1\rangle \leftrightarrow |e\rangle$ using a continuous-wave laser with a variable detuning Δ, and collect the emission from the cavity. To reject the direct reflection of the laser from the sample surface, we spatially separate the excitation and collection by coupling the laser through the notch of the waveguide (see inset of Fig. 2(a)) and collecting the far-field scattered signal from the cavity. We also use a double monochromator to further filter out the laser reflection and spectrally select the emission around transition $|g_2\rangle \leftrightarrow |e\rangle$ within a bandwidth of 120 GHz. We utilize phonon-induced ground state relaxation [37] to perform state reinitialization after emitting a photon.

Figure 3(a) shows the measured emission spectrum as we vary the detuning Δ. We observe two distinct peaks in the measured spectra, labeled as R and S respectively. The emission peak R continuously red shifts as we increase the detuning Δ, corresponding to the cavity-enhanced Raman emission. The emission peak S remains centered around the natural frequency of

$|g_2\rangle \leftrightarrow |e\rangle$, which is due to incoherent excitation of the system into the state $|e\rangle$ followed by spontaneous emission via transition $|e\rangle \rightarrow |g_2\rangle$. We are able to achieve a tuning range of 99 GHz for the Raman emission, which is an order of magnitude larger than the best value achieved previously for a color center [14]. We note that the measured linewidth of both peaks is limited by the double-monochromator (3.5 GHz).
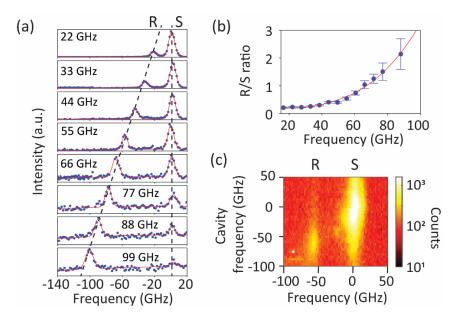

FIG. 3. (Color online) (a) Cavity emission spectra as we vary the excitation detuning Δ. The blue dots show measured data, and the red solid lines show the numerical fits to a double Lorentzian function. The labels R and S represent the Raman and spontaneous emission peaks, respectively. (b) Ratio between the Raman and spontaneous emission intensity as we vary the excitation detuning Δ. The blue circles show measured values, and the red solid line shows numerically calculated ratios. (c) Cavity emission spectra as we tune the cavity across both the spontaneous and Raman emission peaks. In both panels (a) and (c), the frequency values are given in terms of detuning from transition $|g_2\rangle \leftrightarrow |e\rangle$.

Besides an unprecedented tuning bandwidth, the cavity also enables selective enhancement of

Raman emission as we spectrally detune the Raman emission away from the emitter resonance. To quantitatively show this effect, we extract the ratio between the Raman and spontaneous emission intensity (referred as the R/S ratio) at each detuning, as shown in Fig. 3(b). The R/S ratio increases by a factor of 10 when we increase Δ from 15 GHz to 88 GHz. The R/S ratio achieves even higher value at 99 GHz, but we cannot accurately calculate the ratio at this condition due to the vanishing spontaneous emission peak that is too close with the noise floor.

We now verify that the selective enhancement at large detuning originates from the cavity. We fix the excitation detuning at $\Delta = 55\,\text{GHz}$, and finely tune the cavity frequency across both the Raman and spontaneous emission peaks. If the improvement of R/S ratio at large detuning is not related with the cavity, we should observe no dependence of the R/S ratio as we sweep the cavity frequency. In contrast, as shown in Fig. 3(c), when the cavity is resonant at the Raman emission frequency (-55 GHz), we observe at least 10-fold enhancement of the Raman emission intensity compared with the case when the cavity is detuned 100 GHz away from the Raman emission. This 10-fold enhancement is a lower-bound estimate since we did not subtract the background due to laser leakage. The cavity can also enhance the spontaneous emission, but at a different frequency (~0 GHz). These results confirm that the selective enhancement of the Raman emission is enabled by the cavity.

Finally, we investigate the origin of the strong spontaneous emission, especially at small detuning where the cavity selective enhancement is weak. In fact, previous studies have observed similar spontaneous emission [14], but the physical mechanism for this observation has not been explored thoroughly. We quantitatively explain the spontaneous emission by accounting for

interactions between the SiV⁻ center and a phonon reservoir. Specifically, we derive a microscopic

model that quantifies how the state $|e\rangle$ is excited by absorbing both a photon from the driving

field and a phonon from the reservoir, leading to the spontaneous emission.

We start with the Hamiltonian of the driven Λ-system shown in Fig. 1(b), given by

$$\hat{\mathbf{H}}_{sys} = \Delta|e,0\rangle\langle e,0| + \left(\frac{\Omega}{2}|e,0\rangle\langle g_1,0| + g|e,0\rangle\langle g_2,1| + h.c.\right). \tag{1}$$

We model the phonons as a bath of harmonic oscillators, given by

$$\hat{\mathbf{H}}_{bath} = \sum_{\mathbf{k}} \omega_{\mathbf{k}} \mathbf{b}_{\mathbf{k}}^\dagger \mathbf{b}_{\mathbf{k}}. \tag{2}$$

In Eq. (2), $\mathbf{k}$ is the wavevector of each phonon mode, $\omega_{\mathbf{k}}$ is the frequency of the phonon mode

$\mathbf{k}$, and $\mathbf{b}_{\mathbf{k}}$ is the bosonic annihilation operator for the phonon mode $\mathbf{k}$. The interaction

Hamiltonian between the SiV⁻ center and phonons could be written as

$$\hat{\mathbf{H}}_{sys-bath} = \sum_{\mathbf{k}} \left(\mathbf{b}_{\mathbf{k}} + \mathbf{b}_{\mathbf{k}}^\dagger\right)\left(p_{\mathbf{k}}|g_1,0\rangle\langle g_1,0| + q_{\mathbf{k}}|g_2,1\rangle\langle g_2,1| + r_{\mathbf{k}}|e,0\rangle\langle e,0|\right), \tag{3}$$

where $p_{\mathbf{k}}$, $q_{\mathbf{k}}$, and $r_{\mathbf{k}}$ are the deformation coupling strength between the phonon mode $\mathbf{k}$ and the

electronic states $|g_1\rangle$, $|g_2\rangle$, and $|e\rangle$ respectively. Note that here we do not include the phonon-

induced ground state relaxation since this process only determines the number of excitation and

emission cycles per second and does not affect the R/S ratio. We will add this term

phenomenologically in the final master equation [33].

We now derive the electron-phonon interactions in the form of Lindblad operators following a

similar formalism used for semiconductor quantum dots [38,39]. To derive the Lindblad operators,

we first transform the interaction Hamiltonian $\hat{\mathbf{H}}_{sys-bath}$ into the diagonal basis of $\hat{\mathbf{H}}_{sys}$ (Eq. (1)),

and then write it in the rotating reference frame with respect to $\hat{\mathbf{H}}_{sys} + \hat{\mathbf{H}}_{bath}$. We provide the details

of such derivations in the Supplementary Materials [33]. The final master equation is given by

$d\rho_{sys}/dt = -i\left[\hat{\mathbf{H}}_{sys}, \rho_{sys}\right] + L_{phonon}\left(\rho_{sys}\right)$, where ρ_{sys} is the density matrix of the system, and

$L_{phonon}\left(\rho_{sys}\right)$ is the phonon dissipator, given by

$$
\begin{aligned}
L_{phonon}\left(\rho_{sys}\right) = & \frac{g^2 + \left(\Omega/2\right)^2}{\Delta^2} J_1\left(\Delta\right)\left[n_{th}\left(\Delta\right)D\left(|+\rangle\langle-|\right) + \left(1 + n_{th}\left(\Delta\right)\right)D\left(|-\rangle\langle+|\right)\right] \\
& + \frac{g^2 + \left(\Omega/2\right)^2}{\Delta^2} J_2\left(\Delta\right)\left[n_{th}\left(\Delta\right)D\left(|+\rangle\langle d|\right) + \left(1 + n_{th}\left(\Delta\right)\right)D\left(|d\rangle\langle+|\right)\right],
\end{aligned}
\tag{4}
$$

where $D\left(\hat{\mathbf{O}}\right)\rho_{sys} = \hat{\mathbf{O}}\rho_{sys}\hat{\mathbf{O}}^\dagger - \frac{1}{2}\hat{\mathbf{O}}^\dagger\hat{\mathbf{O}}\rho_{sys} - \frac{1}{2}\rho_{sys}\hat{\mathbf{O}}^\dagger\hat{\mathbf{O}}$ is the general Lindblad super-operator for

the collapse operator $\hat{\mathbf{O}}$. Note that here we only elaborate the dissipation through phonons for the

convenience of discussion. The Supplementary Materials contain the complete master equation

[33]. In Eq. (4), the states $|+\rangle$, $|-\rangle$, and $|d\rangle$ are eigenstates of $\hat{\mathbf{H}}_{sys}$, given by

$$
|+\rangle = \frac{\Omega}{2\Delta}|g_1,0\rangle + \frac{g}{\Delta}|g_2,1\rangle + |e,0\rangle,
\tag{5}
$$

$$
|-\rangle = \frac{\Omega/2}{\sqrt{g^2 + \left(\Omega/2\right)^2}}|g_1,0\rangle + \frac{g}{\sqrt{g^2 + \left(\Omega/2\right)^2}}|g_2,1\rangle - \frac{\sqrt{g^2 + \left(\Omega/2\right)^2}}{\Delta}|e,0\rangle.
\tag{6}
$$

$$
|d\rangle = \frac{g}{\sqrt{g^2 + \left(\Omega/2\right)^2}}|g_1,0\rangle - \frac{\Omega/2}{\sqrt{g^2 + \left(\Omega/2\right)^2}}|g_2,1\rangle.
\tag{7}
$$

The parameters $J_1\left(\Delta\right)$ and $J_2\left(\Delta\right)$ are the spectral density of phonons that couple with the

transition $|+\rangle \leftrightarrow |-\rangle$ and $|+\rangle \leftrightarrow |d\rangle$ respectively. The parameter $n_{th}\left(\Delta\right)$ is the number of phonons

per mode, which follows the Bose-Einstein distribution given by $n_{th}\left(\Delta\right) = \left[\exp\left(\Delta/k_B T\right) - 1\right]^{-1}$.

The phonon dissipator in the form of Eq. (4) has a clear physical intuition. It shows how the

system can be populated incoherently into the dressed state $|+\rangle$ from the states $|-\rangle$ or $|d\rangle$ by

absorption of a single phonon from the reservoir. Since $|+\rangle \approx |e\rangle$ in the limit $\Omega, g \ll \Delta$, the incoherent population transfer into the state $|+\rangle$ leads to spontaneous emission from the excited state. Eq. (4) also includes the reverse process where the state $|+\rangle$ decays to the states $|-\rangle$ or $|d\rangle$ by emitting a phonon, but this process has a minor effect since its rate is typically much slower than other decay mechanisms of the excited state $|+\rangle$.

We numerically solve the master equation of the system, and calculate the cavity emission spectrum using the quantum regression theorem [33]. We set all the parameters using experimentally measured values, except for the phonon spectral densities $J_1(\Delta)$ and $J_2(\Delta)$. The exact form of $J_1(\Delta)$ and $J_2(\Delta)$ depends on many parameters such as the strain susceptibility of each electronic state of the SiV$^-$ center, the local strain of each phonon mode, and the phonon frequency dispersion, which is difficult to derive from the first principles. Here, we qualitatively assume a phonon spectral density function of the form $J_{1,2}(\Delta) = \alpha_{1,2}\Delta^n$, where $\alpha_{1,2}$ is a trivial scalar, and n represents a geometric scaling factor that is determined by the structure [28]. For example, for phonons in the bulk $n = 3$, but for surface phonons $n = 2$. The red solid line in Fig. 3(b) shows the calculated R/S ratio using our model. For the best fit, we obtain $n = 0.31 \pm 0.24$. This value is much smaller than the bulk value of 3, suggesting that the nanobeam strongly modifies the phonon spectral density.

In conclusion, we have demonstrated cavity-enhanced Raman emission from a single SiV$^-$ center. The cavity enables an unprecedented frequency tuning range of 99 GHz, which significantly exceeds the typical spectral inhomogeneity of SiV$^-$ centers in nanostructures. We also demonstrate that the cavity selectively enhances only the Raman emission, which is critical for

achieving high-fidelity of photon-mediated many-body interactions. In our current experiment, we employed two orbital ground states to form a Λ-system, which have short lifetimes [37] and thus limit our capability to generate single photons due to fast re-excitation. In order to obtain pure single photons from the Raman emission, we could utilize the spin sublevels of SiV^- centers, which have lifetimes of milli-seconds at cryogenic temperature [40,41] and seconds at milli-Kelvin temperature [21]. The long coherence time of the electron spin may further enable quantum state transfer between single spins and photons through cavity stimulated adiabatic Raman passage [30]. Ultimately, our results represent an important step towards developing chip-integrated quantum circuits and quantum networks that employ multiple solid-state qubits mediated by single photons in a nanophotonic platform.

References

1   O'brien, J. L., Furusawa, A. & Vučković, J. Photonic quantum technologies. *Nature Photonics* **3**, 687 (2009).

2   Aspuru-Guzik, A. & Walther, P. Photonic quantum simulators. *Nature Physics* **8**, 285 (2012).

3   Giovannetti, V., Lloyd, S. & Maccone, L. Advances in quantum metrology. *Nature photonics* **5**, 222 (2011).

4   Briegel, H.-J., Dür, W., Cirac, J. I. & Zoller, P. Quantum repeaters: the role of imperfect local operations in quantum communication. *Physical Review Letters* **81**, 5932 (1998).

5   Cirac, J. I., Zoller, P., Kimble, H. J. & Mabuchi, H. Quantum state transfer and entanglement distribution among distant nodes in a quantum network. *Physical Review Letters* **78**, 3221 (1997).

6   Kimble, H. J. The quantum internet. *Nature* **453**, 1023 (2008).

7   Togan, E., Chu, Y., Trifonov, A., Jiang, L., Maze, J., Childress, L., Dutt, M. G., Sørensen, A. S., Hemmer, P. & Zibrov, A. S. Quantum entanglement between an optical photon and a solid-state spin qubit. *Nature* **466**, 730 (2010).

8   De Greve, K., Yu, L., McMahon, P. L., Pelc, J. S., Natarajan, C. M., Kim, N. Y., Abe, E., Maier, S., Schneider, C. & Kamp, M. Quantum-dot spin–photon entanglement via frequency downconversion to telecom wavelength. *Nature* **491**, 421 (2012).

9   Gao, W., Fallahi, P., Togan, E., Miguel-Sánchez, J. & Imamoglu, A. Observation of entanglement between a quantum dot spin and a single photon. *Nature* **491**, 426 (2012).

10   Sun, S., Kim, H., Solomon, G. S. & Waks, E. A quantum phase switch between a single solid-state spin and a photon. *Nature nanotechnology* **11**, 539-544 (2016).

11   Bernien, H., Hensen, B., Pfaff, W., Koolstra, G., Blok, M., Robledo, L., Taminiau, T., Markham, M., Twitchen, D. & Childress, L. Heralded entanglement between solid-state qubits separated by three metres. *Nature* **497**, 86 (2013).

12   Hensen, B., Bernien, H., Dréau, A. E., Reiserer, A., Kalb, N., Blok, M. S., Ruitenberg, J., Vermeulen, R. F., Schouten, R. N. & Abellán, C. Loophole-free Bell inequality violation using electron spins separated by 1.3 kilometres. *Nature* **526**, 682-686 (2015).

13   Delteil, A., Sun, Z., Gao, W.-b., Togan, E., Faelt, S. & Imamoğlu, A. Generation of heralded entanglement between distant hole spins. *Nature Physics* **12**, 218 (2016).

14   Sipahigil, A., Evans, R., Sukachev, D., Burek, M., Borregaard, J., Bhaskar, M., Nguyen, C., Pacheco, J., Atikian, H. & Meuwly, C. An integrated diamond nanophotonics platform for quantum optical networks. *Science*, aah6875 (2016).

15   Stockill, R., Stanley, M., Huthmacher, L., Clarke, E., Hugues, M., Miller, A., Matthiesen, C., Le Gall, C. & Atatüre, M. Phase-tuned entangled state generation between distant spin qubits. *Physical review letters* **119**, 010503 (2017).

16   Aharonovich, I., Englund, D. & Toth, M. Solid-state single-photon emitters. *Nature Photonics* **10**, 631 (2016).

17   Rogers, L. J., Jahnke, K. D., Teraji, T., Marseglia, L., Müller, C., Naydenov, B., Schauffert, H., Kranz, C., Isoya, J. & McGuinness, L. P. Multiple intrinsically identical single-photon emitters in the solid state. *Nature communications* **5**, 4739 (2014).

18   Sipahigil, A., Jahnke, K. D., Rogers, L. J., Teraji, T., Isoya, J., Zibrov, A. S., Jelezko, F. & Lukin, M. D. Indistinguishable photons from separated silicon-vacancy centers in diamond. *Physical review letters* **113**, 113602 (2014).

19   Neu, E., Steinmetz, D., Riedrich-Möller, J., Gsell, S., Fischer, M., Schreck, M. & Becher, C. Single photon emission from silicon-vacancy colour centres in chemical vapour deposition nano-diamonds on iridium. *New Journal of Physics* **13**, 025012 (2011).

20   Zhang, J. L., Sun, S., Burek, M. J., Dory, C., Tzeng, Y.-K., Fischer, K. A., Kelaita, Y., Lagoudakis, K. G., Radulaski, M. & Shen, Z.-X. Strongly Cavity-Enhanced Spontaneous Emission from Silicon-Vacancy Centers in Diamond. *Nano Letters* **18**, 1360–1365 (2018).

21   Sukachev, D. D., Sipahigil, A., Nguyen, C. T., Bhaskar, M. K., Evans, R. E., Jelezko, F. & Lukin, M. D. Silicon-Vacancy Spin Qubit in Diamond: A Quantum Memory Exceeding 10 ms with Single-Shot State Readout. *Physical review letters* **119**, 223602 (2017).

22   Evans, R. E., Sipahigil, A., Sukachev, D. D., Zibrov, A. S. & Lukin, M. D. Narrow-linewidth homogeneous optical emitters in diamond nanostructures via silicon ion implantation. *Physical Review Applied* **5**, 044010 (2016).

23   Sweeney, T. M., Carter, S. G., Bracker, A. S., Kim, M., Kim, C. S., Yang, L., Vora, P. M., Brereton, P. G., Cleveland, E. R. & Gammon, D. Cavity-stimulated Raman emission from a single quantum dot spin. *Nature Photonics* **8**, 442 (2014).

24   Pursley, B., Carter, S., Yakes, M., Bracker, A. & Gammon, D. Picosecond pulse shaping of single photons using quantum dots. *Nature communications* **9**, 115 (2018).

25   Lee, J., Bennett, A., Stevenson, R. M., Ellis, D. J., Farrer, I., Ritchie, D. A. & Shields, A. J. Multi-dimensional photonic states from a quantum dot. *Quantum Science and Technology* (2018).

26   Lodahl, P., Mahmoodian, S. & Stobbe, S. Interfacing single photons and single quantum dots with photonic nanostructures. *Reviews of Modern Physics* **87**, 347 (2015).

27   Hepp, C., Müller, T., Waselowski, V., Becker, J. N., Pingault, B., Sternschulte, H., Steinmüller-Nethl, D., Gali, A., Maze, J. R. & Atatüre, M. Electronic structure of the silicon vacancy color center in diamond. *Physical Review Letters* **112**, 036405 (2014).

28   Sohn, Y.-I., Meesala, S., Pingault, B., Atikian, H. A., Holzgrafe, J., Gundogan, M., Stavrakas, C., Stanley, M. J., Sipahigil, A. & Choi, J. Engineering a diamond spin-qubit with a nano-electro-mechanical system. *arXiv preprint arXiv:1706.03881* (2017).

29   Meesala, S., Sohn, Y.-I., Pingault, B., Shao, L., Atikian, H. A., Holzgrafe, J., Gundogan, M., Stavrakas, C., Sipahigil, A. & Chia, C. Strain engineering of the silicon-vacancy center in diamond. *arXiv preprint arXiv:1801.09833* (2018).

30   Hennrich, M., Legero, T., Kuhn, A. & Rempe, G. Vacuum-stimulated Raman scattering based on adiabatic passage in a high-finesse optical cavity. *Physical Review Letters* **85**, 4872 (2000).

31   Kuhn, A., Hennrich, M. & Rempe, G. Deterministic single-photon source for distributed quantum networking. *Physical review letters* **89**, 067901 (2002).

32   Keller, M., Lange, B., Hayasaka, K., Lange, W. & Walther, H. Continuous generation of single photons with controlled waveform in an ion-trap cavity system. *Nature* **431**, 1075 (2004).

33   See Supplemental Material at [URL will be inserted by publisher] for detailed theoretical analysis and supporting experimental results.

34   Zhang, J. L., Lagoudakis, K. G., Tzeng, Y.-K., Dory, C., Radulaski, M., Kelaita, Y., Fischer, K. A., Sun, S., Shen, Z.-X. & Melosh, N. A. Complete coherent control of silicon vacancies in diamond nanopillars containing single defect centers. *Optica* **4**, 1317-1321 (2017).

35   Burek, M. J., de Leon, N. P., Shields, B. J., Hausmann, B. J., Chu, Y., Quan, Q., Zibrov, A. S., Park, H., Lukin, M. D. & Lončar, M. Free-standing mechanical and photonic nanostructures in single-crystal diamond. *Nano letters* **12**, 6084-6089 (2012).

36   Burek, M. J., Chu, Y., Liddy, M. S., Patel, P., Rochman, J., Meesala, S., Hong, W., Quan, Q., Lukin, M. D. & Lončar, M. High quality-factor optical nanocavities in bulk single-crystal diamond. *Nature communications* **5**, 5718 (2014).

37   Jahnke, K. D., Sipahigil, A., Binder, J. M., Doherty, M. W., Metsch, M., Rogers, L. J., Manson, N. B., Lukin, M. D. & Jelezko, F. Electron–phonon processes of the silicon-vacancy centre in diamond. *New Journal of Physics* **17**, 043011 (2015).

38   Gauger, E. M., Benjamin, S. C., Nazir, A. & Lovett, B. W. High-fidelity all-optical control of quantum dot spins: Detailed study of the adiabatic approach. *Physical Review B* **77**, 115322 (2008).

39   McCutcheon, D. P. & Nazir, A. Quantum dot Rabi rotations beyond the weak exciton–phonon coupling regime. *New Journal of Physics* **12**, 113042 (2010).

40   Pingault, B., Becker, J. N., Schulte, C. H., Arend, C., Hepp, C., Godde, T., Tartakovskii, A. I., Markham, M., Becher, C. & Atatüre, M. All-optical formation of coherent dark states of silicon-vacancy spins in diamond. *Physical review letters* **113**, 263601 (2014).

41   Rogers, L. J., Jahnke, K. D., Metsch, M. H., Sipahigil, A., Binder, J. M., Teraji, T., Sumiya, H., Isoya, J., Lukin, M. D. & Hemmer, P. All-optical initialization, readout, and coherent preparation of single silicon-vacancy spins in diamond. *Physical review letters* **113**, 263602 (2014).

Supplementary Materials

Cavity-enhanced Raman emission from a single color center in a solid

Shuo Sun, Jingyuan Linda Zhang, Kevin A. Fischer, Michael J. Burek,
Constantin Dory, Konstantinos G. Lagoudakis, Yan-Kai Tzeng, Marina Radulaski,
Yousif Kelaita, Amir Safavi-Naeini, Zhi-Xun Shen, Nicholas A. Melosh,
Steven Chu, Marko Lončar, and Jelena Vučković

1. Derivation of Raman emission rate

We first calculate the Raman emission rate from a Λ-system without a cavity. Figure S1(a) shows the energy level structure of the Λ-system, which consists of two ground states labeled as $|1\rangle$ and $|2\rangle$, and an excited state labeled as $|3\rangle$. We assume that a laser drives the transition $|1\rangle \leftrightarrow |3\rangle$ with a Rabi frequency Ω and a detuning Δ, and generates Raman emission from the transition $|3\rangle \rightarrow |2\rangle$. In a rotating reference frame with respect to the driving laser, the Hamiltonian of the system is given by

$$\hat{\mathbf{H}} = \hbar\Delta\hat{\boldsymbol{\sigma}}_{33} + \hbar\frac{\Omega}{2}\left(\hat{\boldsymbol{\sigma}}_{13} + \hat{\boldsymbol{\sigma}}_{31}\right), \tag{S1}$$

where the operator $\hat{\boldsymbol{\sigma}}_{ij}$ is defined as $\hat{\boldsymbol{\sigma}}_{ij} = |i\rangle\langle j|$ for $i, j \in \{1, 2, 3\}$. The dynamics of the system expectation values can be derived from the Heisenberg-Langevin equations, resulting in

$$\frac{d\langle\hat{\boldsymbol{\sigma}}_{13}\rangle}{dt} = -(i\Delta + \gamma)\langle\hat{\boldsymbol{\sigma}}_{13}\rangle - i\frac{\Omega}{2}\left(\langle\hat{\boldsymbol{\sigma}}_{11}\rangle - \langle\hat{\boldsymbol{\sigma}}_{33}\rangle\right), \tag{S2}$$

$$\frac{d\langle\hat{\boldsymbol{\sigma}}_{33}\rangle}{dt} = -\Gamma_{tot}\langle\hat{\boldsymbol{\sigma}}_{33}\rangle - i\frac{\Omega}{2}\left(\langle\hat{\boldsymbol{\sigma}}_{31}\rangle - \langle\hat{\boldsymbol{\sigma}}_{13}\rangle\right), \tag{S3}$$

$$\frac{d\langle\hat{\boldsymbol{\sigma}}_{22}\rangle}{dt} = \Gamma\langle\hat{\boldsymbol{\sigma}}_{33}\rangle. \tag{S4}$$

In Eqs. (S2) - (S4), γ is the dipole decoherence rate of transition $|1\rangle \leftrightarrow |3\rangle$, Γ is the spontaneous emission rate of the transition $|3\rangle \rightarrow |2\rangle$, Γ_{tot} is the total decay rate of the excited state $|3\rangle$. In the large detuning limit where $\Omega, \Gamma_{tot}, \gamma \ll \Delta$, the excited state $|3\rangle$ is weakly excited. Thus, we can adiabatically eliminate this state by taking the steady-state solution of Eqs. (S2) and (S3). Substituting the steady-state solutions into Eq. (S4), we obtain that

$$\frac{d\langle \hat{\boldsymbol{\sigma}}_{22} \rangle}{dt} = \Gamma \cdot \frac{\alpha}{2\alpha + \Gamma_{tot}} (1 - \langle \hat{\boldsymbol{\sigma}}_{22} \rangle), \tag{S5}$$

where $\alpha = \dfrac{\Omega^2}{2} \cdot \dfrac{\gamma}{\Delta^2 + \gamma^2}$. To obtain Eq. (S5), we used the identity that $\langle \hat{\boldsymbol{\sigma}}_{11} \rangle + \langle \hat{\boldsymbol{\sigma}}_{22} \rangle + \langle \hat{\boldsymbol{\sigma}}_{33} \rangle = 1$

and $\langle \hat{\boldsymbol{\sigma}}_{31} \rangle = \langle \hat{\boldsymbol{\sigma}}_{13} \rangle^\dagger$.
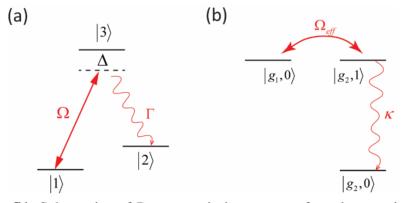

Figure S1. Schematics of Raman emission process for a bare emitter (a) and an emitter that couples to the cavity (b) respectively.

Eq. (S5) has a very clear physical interpretation. It shows that the population of the ground state $|2\rangle$ grows exponentially with a rate $R_0 = \Gamma \cdot \dfrac{\alpha}{2\alpha + \Gamma_{tot}}$, which is exactly the Raman emission rate. To simplify the expression of the Raman emission rate, we assume the ideal

scenario where the excited state $|3\rangle$ decays only to the ground state $|2\rangle$ through spontaneous emission ($\Gamma_{tot} = \Gamma$), and the linewidth of transition $|1\rangle \leftrightarrow |3\rangle$ is lifetime limited ($\gamma = \dfrac{\Gamma}{2}$). This assumption gives the upper bound of the Raman emission rate. Under this assumption, the Raman emission rate is given by $R_0 = \Gamma \cdot \dfrac{\alpha}{2\alpha + \Gamma}$, where $\alpha = \dfrac{\Omega^2}{4} \cdot \dfrac{\Gamma}{\Delta^2 + (\Gamma/2)^2}$. In the large detuning limit where $\Omega, \Gamma \ll \Delta$, we have $\alpha \ll \Gamma$, thus the Raman emission rate is given by

$$R_0 = \alpha = \frac{\Omega^2}{4\Delta^2}\Gamma.$$

Now we calculate the rate of the cavity enhanced Raman emission. As explained in the main text, by adiabatic elimination of the state $|e,0\rangle$, the cavity enhanced Raman emission can be understood as an effective Rabi oscillation between $|g_1,0\rangle$ and $|g_2,1\rangle$, followed by an decay from $|g_2,1\rangle$ to $|g_2,0\rangle$ with a rate κ. Figure S1(b) shows this simplified picture. It is clear that this picture resembles the three-level systems shown in Fig. S1(a), if we define $|1\rangle \equiv |g_1,0\rangle$, $|2\rangle \equiv |g_2,0\rangle$ and $|3\rangle \equiv |g_2,1\rangle$. Therefore, we could calculate the cavity enhanced Raman emission rate R_c following the same derivations shown above, given by $R_c = \dfrac{\Omega_{eff}^2}{\kappa}$, where $\Omega_{eff} = \Omega g/\Delta$ as shown in the main text.

2. Second order correlation measurements

We perform second order correlation measurements to verify that the emission peaks C and D shown in Fig. 2(c) of the main text originate from a single silicon-vacancy (SiV⁻) center. We

excite the device using a 2-ps pulsed laser with a repetition rate of 80 MHz and a center wavelength of 720 nm. We collect the emission using a multi-mode fiber and send it to a Hanbury Brown-Twiss (HBT) intensity interferometer composed of a 50/50 beam-splitter and two Single Photon Counting Modules (SPCMs). We use a time correlated single-photon counting system (PicoHarp 300) to process the detection events from the two SPCMs and obtain the second order correlation. To isolate the emission from peaks C and D respectively, we resonantly couple the cavity with either peak C or D and use the cavity as a spectral filter. Figure S2 shows the measured second order correlations when the cavity is resonant with peak C and D respectively, where τ is the delay time between two detection events obtained by the two SPCMs. We observe strong suppression of the second order correlation near $\tau = 0$ in both cases, confirming that both emission peaks are from a single SiV$^-$ center.
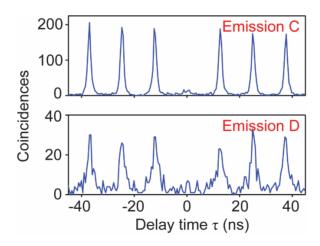

Figure S2. Second order correlations of the SiV$^-$ emission when the cavity is resonant with emission peak C and D respectively.

3. Estimation of Purcell factor

We estimate the Purcell factor F based on the calculated coupling strength, defined as

$F = \dfrac{4g^2/\kappa}{\Gamma_{bare}}$, where Γ_{bare} is the spontaneous emission rate of transition $|e\rangle \rightarrow |g_2\rangle$ when it

decouples with the cavity. For this specific SiV$^-$ center, we expect that $\Gamma_{bare} << 1/\tau_{off}$ because

the excited state $|e\rangle$ emits 10 times stronger through the transition $|e\rangle \rightarrow |g_1\rangle$ compared with

transition $|e\rangle \rightarrow |g_2\rangle$ (see Fig. 2(c)). In addition, the excited state might also decay through

non-radiative processes or phonon-sideband emission. By assuming a higher-bound quantum

yield of $\eta_{radiative} = 30\%$ and a zero-phonon-line emission fraction of $\eta_{ZPL} = 80\%$, we could

calculate the higher-bound of Γ_{bare} given by $\Gamma_{bare} = \eta_{radiative} \cdot \eta_{ZPL} \cdot \eta_D \dfrac{1}{\tau_{off}} = 2\pi \times 2.1\,\text{MHz}$,

where $\eta_D = 10\%$ is the fraction of the zero-phonon-line emission into transition $|e\rangle \rightarrow |g_2\rangle$. We

thus estimate the lower-bound of the Purcell factor to be $F = \dfrac{4g^2/\kappa}{\Gamma_{bare}} = 22.7$.

4. Complete derivation of system master equation

We first derive the Lindblad operator for the electron-phonon interaction Hamiltonian

$\hat{\mathbf{H}}_{sys-bath}$. To do that we have to first write the interaction Hamiltonian $\hat{\mathbf{H}}_{sys-bath}$ in the diagonal

basis of $\hat{\mathbf{H}}_{sys}$ (Eq. (1) of the main text), and then write it in the rotating reference frame with

respect to $\hat{\mathbf{H}}_{sys} + \hat{\mathbf{H}}_{bath}$. In the diagonal basis, we can write $\hat{\mathbf{H}}_{sys}$ as

$$\hat{\mathbf{H}}_{sys} = \omega_+ |+\rangle\langle+| + \omega_- |-\rangle\langle-| + \omega_d |d\rangle\langle d|, \tag{S6}$$

where the eigenstates $|+\rangle$, $|-\rangle$, and $|d\rangle$ are given by Eqs. (5) – (7) in the main text, the

eigenfrequencies ω_+, ω_-, and ω_d are given by $\omega_+ = \Delta + \dfrac{\left(\Omega/2\right)^2 + g^2}{\Delta}$, $\omega_- = -\dfrac{\left(\Omega/2\right)^2 + g^2}{\Delta}$,

and $\omega_d = 0$ respectively. In the rotating reference frame with respect to $\hat{\mathbf{H}}_{sys} + \hat{\mathbf{H}}_{bath}$, we could

rewrite $\hat{\mathbf{H}}_{sys-bath}$ as

$$\hat{\mathbf{H}}_{sys-bath} = \frac{\sqrt{g^2 + \left(\Omega/2\right)^2}}{\Delta} \sum_{\mathbf{k}} \mathbf{b}_{\mathbf{k}} \left(x_{\mathbf{k}} |+\rangle\langle-| e^{i(\Lambda_1 - \omega_{\mathbf{k}})t} + y_{\mathbf{k}} |+\rangle\langle d| e^{i(\Lambda_2 - \omega_{\mathbf{k}})t} \right) + h.c., \qquad (S7)$$

where Λ_1 and Λ_2 are given by $\Lambda_1 = \omega_+ - \omega_-$ and $\Lambda_2 = \omega_+ - \omega_d$ respectively, $x_{\mathbf{k}}$ and $y_{\mathbf{k}}$

are given by $x_{\mathbf{k}} = p_{\mathbf{k}} \dfrac{\left(\Omega/2\right)^2}{g^2 + \left(\Omega/2\right)^2} + q_{\mathbf{k}} \dfrac{g^2}{g^2 + \left(\Omega/2\right)^2} - r_{\mathbf{k}}$ and $y_{\mathbf{k}} = \left(p_{\mathbf{k}} - q_{\mathbf{k}}\right) \dfrac{g\left(\Omega/2\right)}{g^2 + \left(\Omega/2\right)^2}$

respectively. To obtain Eq. (S7), we have utilized the rotating wave approximation to keep only

the slowly varying terms. We eliminate the phonon coupling terms with the operators $|+\rangle\langle+|$,

$|-\rangle\langle-|$, and $|d\rangle\langle d|$ because they interact with phonons at zero frequency where phonon density

of states vanishes. Similarly, we eliminate the phonon coupling terms with the operators $|d\rangle\langle-|$,

and $|-\rangle\langle d|$ because they interact with phonons at a low frequency near $\omega_d - \omega_- = \dfrac{\left(\Omega/2\right)^2 + g^2}{\Delta}$,

which is in the order of 100 MHz. Such frequencies correspond to a phonon wavelength longer

than 10 µm, which cannot exist in our nanobeam structure.

Now we can derive a master equation by integrating the von Neumann equation for the

density matrix ρ of the joint system and phonon bath, and then tracing over the phonon modes,

given by

$$\frac{d\rho_{sys}}{dt} = -\int_0^t \text{tr}_{bath}\left(\left[\hat{\mathbf{H}}_{sys-bath}\left(t\right),\left[\hat{\mathbf{H}}_{sys-bath}\left(t'\right),\rho\left(t'\right)\right]\right]\right)dt'. \tag{S8}$$

We make the Born-Markov approximation, which allows us to substitute $\rho\left(t'\right)$ with $\rho\left(t\right)$ and

write it as $\rho = \rho_{sys} \otimes \rho_{bath}$. These assumptions result in a master equation given by

$$\frac{d\rho_{sys}}{dt} = -\int_0^t \text{tr}_{bath}\left(\left[\hat{\mathbf{H}}_{sys-bath}\left(t\right),\left[\hat{\mathbf{H}}_{sys-bath}\left(t\right),\rho_{sys}\left(t\right)\otimes\rho_{bath}\right]\right]\right)dt'. \tag{S9}$$

We further rewrite $\hat{\mathbf{H}}_{sys-bath}$ as $\hat{\mathbf{H}}_{sys-bath} = \hat{\mathbf{H}}^{(1)}_{sys-bath} + \hat{\mathbf{H}}^{(2)}_{sys-bath}$, where $\hat{\mathbf{H}}^{(1)}_{sys-bath}$ and $\hat{\mathbf{H}}^{(2)}_{sys-bath}$ are

given by

$$\hat{\mathbf{H}}^{(1)}_{sys-bath} = \frac{\sqrt{g^2 + \left(\Omega/2\right)^2}}{\Delta}\sum_{\mathbf{k}} x_{\mathbf{k}}\mathbf{b}_{\mathbf{k}}\left|+\right\rangle\left\langle-\right|e^{i\left(\Lambda_1 - \omega_{\mathbf{k}}\right)t} + h.c., \tag{S10}$$

$$\hat{\mathbf{H}}^{(2)}_{sys-bath} = \frac{\sqrt{g^2 + \left(\Omega/2\right)^2}}{\Delta}\sum_{\mathbf{k}} y_{\mathbf{k}}\mathbf{b}_{\mathbf{k}}\left|+\right\rangle\left\langle d\right|e^{i\left(\Lambda_2 - \omega_{\mathbf{k}}\right)t} + h.c.. \tag{S11}$$

Since $\hat{\mathbf{H}}^{(1)}_{sys-bath}$ and $\hat{\mathbf{H}}^{(2)}_{sys-bath}$ involves interaction with phonons of different frequencies

separated by ~100 MHz, they cannot interact with the same phonon mode. Therefore, we could

further rewrite Eq. (S9) as

$$\frac{d\rho_{sys}}{dt} = -\sum_{m=1}^{2}\int_0^t \text{tr}_{bath}\left(\left[\hat{\mathbf{H}}^{(m)}_{sys-bath},\left[\hat{\mathbf{H}}^{(m)}_{sys-bath},\rho_{sys}\left(t\right)\otimes\rho_{bath}\right]\right]\right)dt'. \tag{S12}$$

This leads to the final master equation given by $\frac{d\rho_{sys}}{dt} = -i\left[\hat{\mathbf{H}}_{sys},\rho_{sys}\right] + \sum_{m=1}^{2}L^{(m)}_{phonon}\left(\rho_{sys}\right)$, where

$L^{(1)}_{phonon}\left(\rho_{sys}\right)$ and $L^{(2)}_{phonon}\left(\rho_{sys}\right)$ are given by

$$L^{(1,2)}_{phonon}\left(\rho_{sys}\right) = \frac{g^2 + \left(\Omega/2\right)^2}{\Delta^2}J_{1,2}\left(\Lambda_{1,2}\right)\left[n_{th}\left(\Lambda_{1,2}\right)D\left(\left|+\right\rangle\left\langle-\right|\right) + \left(1 + n_{th}\left(\Lambda_{1,2}\right)\right)D\left(\left|-\right\rangle\left\langle+\right|\right)\right], \tag{S13}$$

where $J_{1,2}\left(\Lambda_{1,2}\right)$ is the phonon spectral density given by $J_1\left(\Lambda_1\right) = 2\pi\sum_{\mathbf{k}}\left|x_{\mathbf{k}}\right|^2\delta\left(\omega_{\mathbf{k}} - \Lambda_1\right)$ and

$J_2\left(\Lambda_2\right) = 2\pi\sum_{\mathbf{k}}\left|y_{\mathbf{k}}\right|^2\delta\left(\omega_{\mathbf{k}} - \Lambda_2\right)$ respectively, and $n_{th}\left(\Lambda_{1,2}\right)$ is the number of phonons per

mode, which follows the Bose-Einstein distribution given by $n_{th}\left(\Lambda_{1,2}\right)=\left[\exp\left(\Lambda_{1,2}/k_B T\right)-1\right]^{-1}$.

Since both the phonon spectral density $J_{1,2}\left(\Lambda_{1,2}\right)$ and the thermal distribution function $n_{th}\left(\Lambda_{1,2}\right)$ are relatively flat as a function of phonon frequency, and $\Lambda_{1,2}\approx\Delta$ in the limit $\Omega, g \ll \Delta$, we could approximately write $J_{1,2}\left(\Lambda_{1,2}\right)$ and $n_{th}\left(\Lambda_{1,2}\right)$ as $J_{1,2}\left(\Lambda_{1,2}\right)=J_{1,2}\left(\Delta\right)$ and $n_{th}\left(\Lambda_{1,2}\right)=n_{th}\left(\Delta\right)$ respectively. This gives the phonon dissipator provided as Eq. (4) in the main text.

In our numerical simulation, we use the full master equation that account for all possible dissipation mechanisms, given by $\dfrac{d\rho_{sys}}{dt}=-i\left[\hat{\mathbf{H}}_{sys},\rho_{sys}\right]+L_{phonon}\left(\rho_{sys}\right)+L_{cav}\left(\rho_{sys}\right)+L_{SiV}\left(\rho_{sys}\right)$, where $L_{cav}\left(\rho_{sys}\right)=\kappa D(\hat{\mathbf{a}})$ is the cavity decay, and $L_{SiV}\left(\rho_{sys}\right)$ is the decay of the SiV$^-$ center, given by

$$L_{SiV}\left(\rho_{sys}\right)=\gamma_1 D\left(|g_1\rangle\langle e|\right)+\gamma_2 D\left(|g_2\rangle\langle e|\right)+\gamma_{flip}D\left(|g_1\rangle\langle g_2|\right), \tag{S12}$$

where γ_1 and γ_2 are decay rates from the excited state $|e\rangle$ to the ground states $|g_1\rangle$ and $|g_2\rangle$ respectively, γ_{flip} is the decay rate from $|g_2\rangle$ to $|g_1\rangle$. We do not include the state flipping from $|g_1\rangle$ to $|g_2\rangle$ in the Liouvillian superoperator, because this process requires absorption of a phonon at $\delta_g/2\pi=544\,\mathrm{GHz}$ that is much larger than the value $k_B T/2\pi=83\,\mathrm{GHz}$, and therefore is much slower than its reverse process.

We numerically solve the master equation of the system and calculate the cavity emission spectrum using the quantum regression theorem. We fix g and κ using experimentally measured values given by $g/2\pi=0.80\,\mathrm{GHz}$ and $\kappa/2\pi=53.7\,\mathrm{GHz}$. We assume that the decay

rates from the excited state $|e\rangle$ to the ground states $|g_1\rangle$ and $|g_2\rangle$ are identical, thus we have

$$\gamma_1 = \gamma_2 = \frac{1}{2\tau_{off}} = 2\pi \times 0.046\,\text{GHz}.$$ This assumption is valid since the dominant decay mechanism

of the excited state is through a non-radiative process [1], which rate is irrelevant of the final

ground state. To determine the driving Rabi frequency Ω, we resonantly drive transition

$|g_1\rangle \leftrightarrow |e\rangle$, and measure the fluorescence intensity as we vary the driving laser power. This

measurement allows us to obtain the saturation power for transition $|g_1\rangle \leftrightarrow |e\rangle$, enabling us to

determine the driving Rabi frequency based on the measured laser power. In our experiment, we

use a driving Rabi frequency of $\Omega/2\pi = 2.58\,\text{GHz}$. The only parameter we cannot determine is

γ_{flip}. However, as we verified numerically, the value of γ_{flip} only determines the number of

excitation and emission cycles per second – it does not affect the R/S ratio. In the calculation we

simply fix γ_{flip} to be $\gamma_{flip}/2\pi = 0.8\,\text{GHz}$ based on an estimate from a previous literature [2].

References

1 Jahnke, K. D., Sipahigil, A., Binder, J. M., Doherty, M. W., Metsch, M., Rogers, L. J., Manson, N. B., Lukin, M. D. & Jelezko, F. Electron–phonon processes of the silicon-vacancy centre in diamond. *New Journal of Physics* **17**, 043011 (2015).

2 Sohn, Y.-I., Meesala, S., Pingault, B., Atikian, H. A., Holzgrafe, J., Gundogan, M., Stavrakas, C., Stanley, M. J., Sipahigil, A. & Choi, J. Engineering a diamond spin-qubit with a nano-electro-mechanical system. *arXiv preprint arXiv:1706.03881* (2017).